Laser-Ablation-Based Ion Source Characterization and Manipulation for Laser-Driven Ion Acceleration

Sommer, P.; Metzkes, J.; Brack, F.-E.; Cowan, T. E.; Kraft, S. D.; Obst, L.; Rehwald, M.; Schlenvoigt, H.-P.; Schramm, U.; Zeil, K.;

Originally published:

March 2018

Plasma Physics and Controlled Fusion 60(2018)5, 054002

DOI: https://doi.org/10.1088/1361-6587/aab21e

Laser-ablation-based ion source characterization and manipulation for laser-driven ion acceleration

Laser-Ablation-Based Ion Source Characterization and Manipulation for Laser-Driven Ion Acceleration

P. Sommer[1], J. Metzkes-Ng[1], F.-E. Brack[1,2], T. E. Cowan[1,2], S. D. Kraft[1], L. Obst[1,2], M. Rehwald[1,2], H.-P. Schlenvoigt[1], U. Schramm[1,2], K. Zeil[1]

[1]Helmholtz-Zentrum Dresden – Rossendorf (HZDR), Bautzner Landstr. 400, 01328 Dresden, Germany

[2]Technische Universität Dresden, 01062 Dresden, Germany

E-mail: j.metzkes@hzdr.de

Abstract. For laser-driven ion acceleration from thin foils ($\sim 10\,\mu$m - 100 nm) in the target normal sheath acceleration (TNSA) regime, the hydro-carbon contaminant layer at the target surface generally serves as the ion source and hence determines the accelerated ion species, i.e. mainly protons, carbon and oxygen ions. The specific characteristics of the source layer - thickness and relevant lateral extent - as well as its manipulation have both been investigated since the first experiments on laser-driven ion acceleration using a variety of techniques from direct source imaging to knife-edge or mesh imaging.

In this publication, we present an experimental study in which laser ablation in two fluence regimes (low: $F \sim 0.6\,J/cm^2$, high: $F \sim 4\,J/cm^2$) was applied to characterize and manipulate the hydro-carbon source layer. The high-fluence ablation in combination with a timed laser pulse for particle acceleration allowed for an estimation of the relevant source layer thickness for proton acceleration. Moreover, from these data and independently from the low-fluence regime, the lateral extent of the ion source layer became accessible.

PACS numbers:

1. Introduction

Ion acceleration in laser-driven plasmas is currently investigated as a potential source for energetic ion beams (see review in [1]). The most robust and established among the laser-plasma-based acceleration schemes is target normal sheath acceleration (TNSA) [2, 3, 4]. In TNSA, a relativistic laser pulse ($I > 10^{18}\,\mathrm{W/cm^2}$) interacts with a $\sim 10\,\mu$m - 100 nm thick (target) foil, the surface of which is ionized and turned into a plasma in the interaction region. Free plasma electrons then gain MeV energies in the intense laser field. They are injected into the over-dense target volume and set up charge-separation fields as they form a so-called *Debye sheath* in the vacuum region close ($\sim \mu$m distance) to the target surface. The field strength increases with the electron density n_e and mean electron energy or *hot electron temperature* T_e in the Debye sheath, which is responsible for TNSA of ions. The ion source is the ≈ 1 nm thick [5, 6] contaminant layer (water, hydro-carbons) that is inherently covering the target surface under experimental conditions. The layer's constituents (H, C, O) are field-ionized in the sheath field [7] up to the highest charge state for which the appearance intensity is below the maximum local sheath field strength. In the acceleration process, the charge-to-mass ratio (q/m) of different ion species in combination with screening effects determines that protons ($q/m = 1$) are accelerated most efficiently [8].

Experimental investigations regarding the detailed properties of the source layer started around the first TNSA observation, firstly confirming that the most energetic ions in TNSA originate from the non-laser-irradiated target rear surface [9, 5, 10]. Moreover, the lateral extent of the source layer area (source size) at the target rear surface contributing particles to the accelerated ion distribution was characterized. A summary of the published data is given in Tab. 1. The difficulties in accessing the $\sim 100\,\mu$m - 1 mm source size lie in the transient nature of the TNSA process (picosecond timescales), the small spatial scales of the relevant source area ($\sim$ nm thickness) and in the ion energy dependence of the source size. The latter follows from the radial field strength distribution in the Debye sheath [11].

Knowledge of the actual source size is highly relevant for an understanding of laser-driven ion acceleration regarding firstly, the emission pattern of shaped targets as e.g. reduced-mass or wire targets [12]. Secondly, the spectral width of an accelerated proton distribution was shown to correlate with the lateral extent of the ion source layer with respect to the sheath field size, a proper matching enabling the generation of quasi-monoenergetic proton distributions [13, 14]. On the other hand, removal of the hydro-carbon contaminant layer by laser ablation [13, 14, 15], resistive heating [7, 8] or ion sputtering [5] has been shown to suppress the otherwise dominant acceleration of protons in favor of heavier ions.

In this publication, we present experimental results on the ion source size characterization and manipulation in the TNSA regime using nanosecond laser pulses in a low ($\mathrm{F} \sim 0.6\,\mathrm{J/cm^2}$) and high ($\mathrm{F} \sim 4\,\mathrm{J/cm^2}$) fluence regime for the removal of the hydro-carbon contaminant on the target surface. In the high-fluence case, we found that the

Table 1. Summary of publications presenting experimental data on source size measurements for laser-driven ion acceleration in the TNSA regime. The derived source size is the proton energy-dependent diameter. Publications in bold print refer to experiments with ultra-short pulse ($\tau \leq 100\,\mathrm{fs}$) drive laser systems for the TNSA process.

Publication	Method	Derived Source Size
Snavely *et al.*, 2000 [3]	penumbral shadowing	$400\,\mu$m
Roth *et al.*, 2002 [17]	direct surface imaging	$300\,\mu$m (3 MeV p^+) $80\,\mu$m (10 MeV p^+)
Patel *et al.*, 2003 [18]	direct surface imaging	250 - 80 μm (4 - 12 MeV p^+)
Cowan *et al.*, 2004 [16, 19, 20]	direct surface imaging	$< 15\,\mu$m (> 10 MeV p^+)
Borghesi *et al.*, 2004 [21]	mesh imaging/back projection	$\sim 100\,\mu$m (15 MeV p^+)
Schreiber *et al.*, 2004 [22]	knife edge	> 550 - $< 80\,\mu$m (0.5 - 2 MeV p^+)
Schreiber *et al.*, 2006 [23]	spectrometer pinhole imaging	$\sim 100\,\mu$m (0.2 - 4 MeV p^+)
Brambrink 2006 [24]	direct surface imaging	$\sim 100\,\mu$m (6 - 12 MeV p^+)
Roth *et al.*, 2006 [25]	direct surface imaging	90 - 40 μm (3 - 11 MeV p^+)
McKenna *et al.*, 2007 [26]	spectrometer pinhole imaging	$\sim$ mm size
TerAvetisyan *et al.*, 2009 [27]	spectrometer with multi-pinhole array imaging	$20\,\mu$m (≈ 4 MeV p^+)

arrival timing of the ablation laser pulse and the laser pulse for particle acceleration on target can be used to suppress the acceleration of protons while enhancing the acceleration of heavier ions. From the fact that the surface cleaning from hydro-carbon contaminants is a transient effect and the proton signal recovers once the delay between the ablation and the acceleration pulse exceeds the timescale of ~ 10 ms, the necessary thickness and lateral extent of the source layer for TNSA can be estimated.

In a second part of the publication, the spatially selective removal of the contaminant layer with lower-fluence ablation pulses is applied to estimate the lateral extent of the proton source size at the target rear surface. The ablation-based approach for the source size measurement is attractive as it employs direct surface imaging but in contrast to surface imaging with e.g. grooved targets [16], no special target surface engineering is required. The method can hence be applied to, e.g. reduced-mass targets or other specially shaped target configurations.

2. Experimental Setup

The reported experiments were performed at the 150 TW dual CPA Draco laser facility at the Helmholtz-Zentrum Dresden – Rossendorf (HZDR). Draco is a Ti:Sapphire laser system that delivers ultra-short pulses of 30 fs duration after compression. It was used at a pulse energy of up to 3 J on target for this experiment. The pulses were focused to an on-target spot size of 3 μm FWHM, amounting to an intensity of about 10^{21} W/cm^2. The high-intensity laser pulses from Draco enabling particle acceleration will be referred to as *acceleration pulses* in the following.

The experimental setup for the laser proton acceleration experiments with target preparation through laser ablation is shown in Fig. 1a. Large titanium foils with 2 μm and 4 μm thickness were used as targets. These were irradiated with the Draco laser under normal incidence. Target surface preparation was done *in situ* via laser ablation with nanosecond laser pulses (12 ns FWHM), delivered by a frequency-doubled Nd:YAG system (CFR 200, Quantel) with a maximum output energy of 150 mJ at 532 nm wavelength. The laser operates on a 10 Hz basis for the use of ablation shot bursts. In the setup, the target front and rear surface could be irradiated by the ablation laser individually as well as simultaneously from the same light source. The ablation beams with near-Gaussian beam profiles were weakly focused to a spot size of approximately 550 μm $\times$ 450 μm FWHM (Fig. 1b) and irradiated the target under oblique incidence ($\sim 25^\circ$ angle of incidence to the target normal). The ablation pulse energy and hence fluence on target was adjusted with a variable attenuator consisting of a wave-plate and a thin film polarizer. The synchronization between the high-intensity pulse and the ablation pulse was done electronically and the delay could be adjusted between synchronization‡ and 90 ms with an accuracy of a few nanoseconds.

The energy- and angle-resolved proton beam profiles of the particle pulses emitted from the target rear surface were recorded with stacks of radiochromic films (RCF) mounted 55 mm away from the target rear surface in target normal direction. Through a hole in the stacks, the energy spectrum of all ion species present in the accelerated particle distribution was measured with higher resolution but in a small solid angle (0.02 μsr) in a Thomson parabola (TP) spectrometer $\sim$ 60 cm downstream from the target. In combination with a microchannel plate detector and a CCD camera, the TP served as an online diagnostic tool for the ions emitted in target normal direction in an energy range of 2 MeV to 30 MeV.

‡ Note that the maximum of the nanosecond long ablation pulse is synchronized with the much shorter main pulse of Draco. Thus the rising edge of the ablation pulse reaches the target surface a few nanoseconds before the main pulse and the ablation process (removal the contamination layer from the target) has already started.

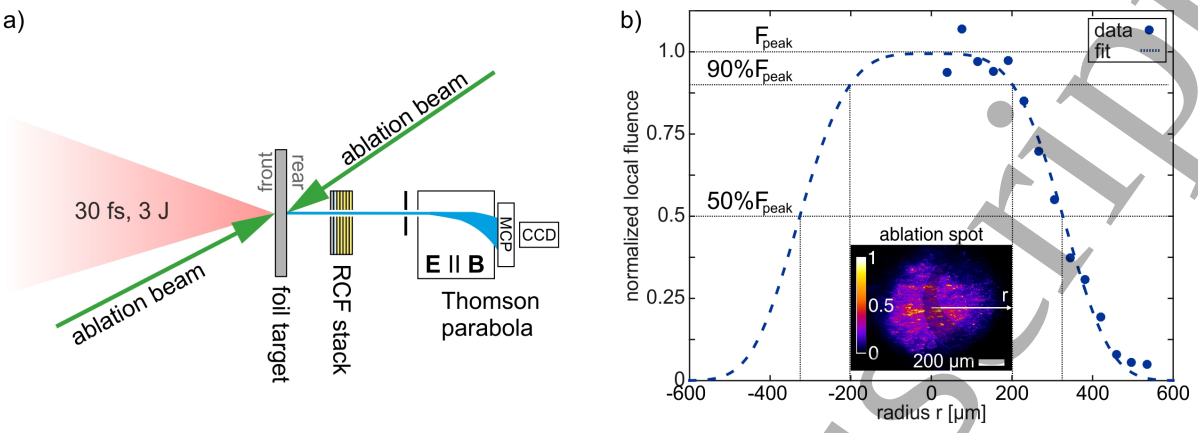

Figure 1. Experimental setup and ablation spot. a) Sketch of the experimental setup. b) Normalized local fluence in the ablation spot for an ablation pulse energy of $\approx 1.3\,\mathrm{mJ}$. The local fluence is the energy contained in a ring with outer radius r and inner radius (r-70 μm) divided by the ring area, i.e. the mean fluence in a concentric ring around the beam center. The measured data are represented for $r > 0$. The fit to the data which is also plotted for $r < 0$ functions as a line to guide the eye. Inset: False-color image of the ablation spot. To record the spatial profile as shown, the ablation beam was focused onto a foil and the scattered light was imaged.

3. Optimization of the Ablation Procedure and Parameters

In situ removal of the hydro-carbon contaminant layer on target foils for laser-driven ion acceleration using nanosecond long ablation pulses in the visible wavelength range operates via photo-thermal processes, i.e. the material melts and evaporation of material occurs from the liquid [28, 29]. Due to the minimum amount of absorbed energy required for evaporation of the irradiated surface, a threshold fluence for ablation F_{thr} exists [28, 29]: $F_{thr} = \rho \cdot \Omega \cdot \sqrt{D \cdot \tau}$, with the density ρ, specific heat of evaporation Ω and heat diffusion coefficient D of the ablated material as well as the ablation pulse duration τ. For the single-shot ablation of the hydro-carbon contaminant layer on a titanium foil with nanosecond long ablation pulses, Pfotenhauer *et al.* [14] experimentally found a threshold fluence of $F_{thr} = (1.2 \pm 0.3)\,\mathrm{J/cm^2}$. F_{thr} was determined via the suppression of the proton signal in the accelerated particle distribution [14], and the same measure will be used in the following. In the presented experimental study, two different ablation regimes were investigated: a low-fluence regime with $F \sim 0.6\,\mathrm{J/cm^2}$ and a high-fluence regime with $F \sim 4\,\mathrm{J/cm^2}$. In the high-fluence regime with $F > F_{thr}$, the hydro-carbon contamination layer is removed in a single ablation shot. Post-ablation characterization of the foils with an optical and a scanning electron microscope (SEM) verified that the applied ablation fluence melted the surface but was low enough to exclude severe damage of the foil (e.g. deformation or creation of holes in the foil).

In the low-fluence regime, $F < F_{thr}$ for single-shot ablation and target cleaning was achieved using a burst of ablation pulses. Multi-pulse effects (incubation) started to occur for 2-pulse bursts in the experiment. The experiment was however performed

Table 2. Summary of publications presenting experimental data on source layer thickness and constituents for laser-driven ion acceleration in the TNSA regime.

Publication	Method	Source Layer Characteristics
Allen *et al.*, 2004 [5]	photoemission spectroscopy	thickness: 1.2 nm layer constituents: $\sim$60% CH_2, 12% H_2O
Steinke *et al.*, 2010 [6]	elastic recoil detection analysis (ERDA)	thickness: 1 nm

with 95 ablation pulses irradiating the target prior to the acceleration pulse as this choice ensured operation in a saturation regime.

The ablation pulse spot size (Fig. 1b) for both the high- and low-fluence regime was chosen such that the proton signal yielded with ablation was considerably reduced compared to the case without ablation (see e.g. the proton spectrum for $\tau_d = 0$ in Fig. 2a).

The delay of the high-intensity acceleration pulse with respect to the (last) ablation pulse was scanned between synchronization and 90 ms for the high-fluence case. Details are discussed in Sec. 4. In agreement with Pfotenhauer *et al.* [14], the delay between the ablation and the acceleration pulse was set to 5 ms for the low-fluence case.

4. Contaminant Layer Growth Time Scales and Acceleration of Heavier Ions

In the high-fluence ablation regime, the ion species and charge state distribution in the accelerated particle pulse was investigated as a function of the temporal delay τ_d between an ablation pulse applied at the target rear surface and the acceleration laser pulse. Exemplary proton spectra recorded with the TP for different τ_d are summarized in Fig. 2, showing that in the case of particle acceleration without an ablation pulse (reference case), a TNSA-like exponential spectrum with a cut-off energy of $\sim$12 MeV is observed. From $\tau_d = 0$ (synchronization) and up to $\tau_d \approx 100\,\mu$s, the proton cut-off energy is decreased by more than 50%. Proton spectra recorded close to synchronization are strongly modulated and the particle number recorded in the TP is reduced by about a factor 5. The observed reduction in proton signal is in agreement with the observations in other ablation experiments [14].

The suppression of efficient proton acceleration for short τ_d is accompanied by an enhanced acceleration of heavier ions (oxygen, titanium), occurring for $\tau_d \leq 1\,\mu$s. This effect is illustrated in Fig. 3 with representative TP raw data for the reference case (without ablation) and different τ_d cases. The data also show that for longer delays τ_d, the acceleration performance for protons recovers and the signal of heavier ions disappears. Fig. 2b quantifies the effect comparing the cut-off energy of C^{4+} ions and

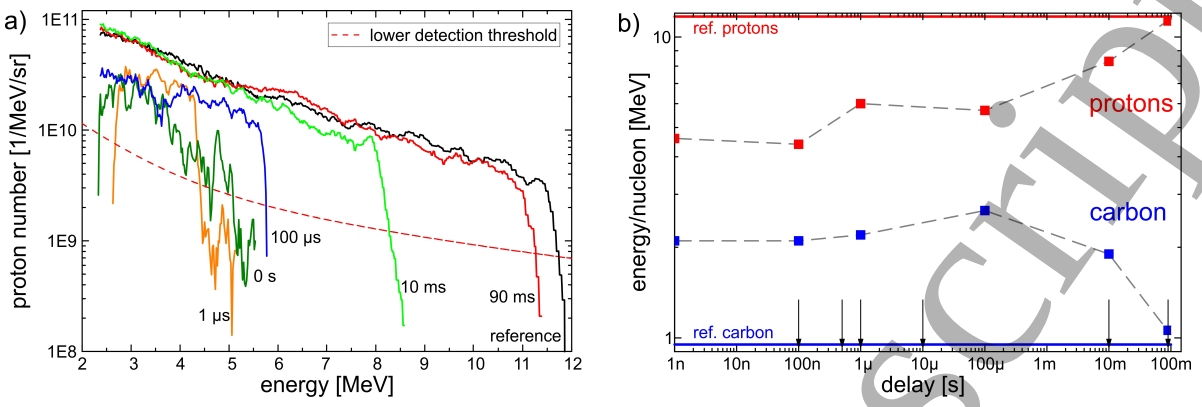

Figure 2. High ablation fluence case - proton and carbon ion behavior. Development of the proton and C^{4+} ion cut-off energies as a function of the delay between the ablation pulse and the high-power acceleration pulse. a) Representative proton spectra measured with the TP for different delay times τ_d. b) Delay-dependence of the maximum energies of protons and C^{4+} ions. The red/blue horizontal lines mark the maximum energy for protons/carbons in the reference case. The arrows mark the delays for which TP raw data are shown in Fig. 3.

protons as a function of τ_d. It confirms that the recovery of the reference case starts at $\tau_d > 100\,\mu$s and is hence slower than the τ_d range for e.g. the efficient titanium ion acceleration (see Fig. 3).

4.1. Acceleration of Heavier Ions

Several experimental studies on laser-driven ion acceleration have shown that the removal of the hydro-carbon contaminant layer enhances the yield of heavier ions from the target bulk. This effect occurs when the normally very efficient ionization and acceleration of protons (low appearance intensity, highest charge-to-mass ratio) and hence their screening of the accelerating field for heavier ions is suppressed [7, 8, 14]. The scanning of the delay τ_d between the ablation and acceleration pulse as performed in the presented experiment gives however a more detailed insight into the source dynamics. The enhanced acceleration of titanium and oxygen only occurs in the small time window of $0 < \tau_d < 1\,\mu$s (Fig. 3), followed by a phase in which mainly the signal of C^{4+} ions and protons is observed and the recovery of the reference case is taking place ($100\,\mu\text{s} < \tau_d < 90\,\text{ms}$). A possible explanation for these two phases and respective timescales is the following: Whereas the source for the carbon and proton signal is in fact the hydro-carbon contaminant layer, the oxygen and titanium ions originate from a titanium oxide layer on the foil surface. The suppression and recovery behavior of the C^{4+} ion versus proton signal might be due to an interplay of a spatial de-mixing of both ion species in the source layer due to ablation and multi-species effects in the acceleration phase. Multi-species effects are indicated by the C^{4+} ion trace: Whereas it is continuous for the reference case as well as after recovery ($\tau_d \sim 90\,\text{ms}$), the lower

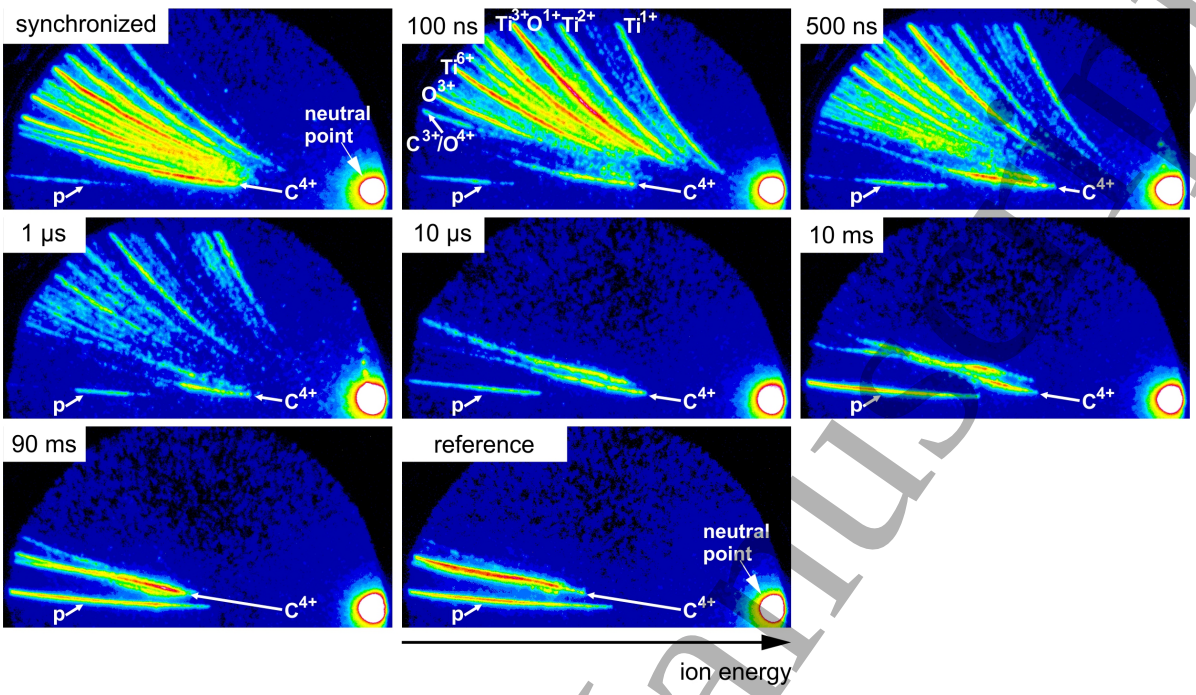

Figure 3. High ablation fluence case - acceleration of heavier ions. Development of the proton and ion species content in the accelerated distribution as a function of the delay τ_d between the ablation pulse and the high-power acceleration pulse. Raw data from the TP are shown, illustrating the occurrence delay-dependent acceleration of heavier ions.

energies are missing for all other $\tau_d < 1\,\mathrm{ms}$ (compare [8, 31]).

4.2. Source Layer Recovery

In contrast to e.g. resistive heating for target cleaning [7, 8], the application of nanosecond ablation pulses allows for a dynamic alteration of the accelerated ion species via the ablation and acceleration pulse timing τ_d. Characterization of the proton acceleration (achieved cut-off energy and yield) as a function of τ_d can be used to estimate the necessary contaminant layer thickness that enables particle acceleration as in the reference case.

Starting point for the estimation is the experimentally derived recovery time of 90 ms to re-establish the contaminant layer conditions as in the reference case (Fig. 3). The recovery process of the contaminant layer on the target surface is modeled as re-adsorption from a gas phase at pressure p and temperature T with molecules of mass m in front of the surface. For the impact rate R of molecules per area per time then holds $R = p/\sqrt{3mk_BT}$. Each molecule hitting the surface is considered as permanently adsorbed (compare [14]). Assuming $p = 10^{-5}$ mbar and room temperature, the growth time for the commonly present contaminant layer of 1.2 nm thickness (Tab. 2) is 6 s [14]. The strongly decreased recovery time of $\tau_{rec} \approx 90\,\mathrm{ms}$ measured in the presented

experiment could indicate an increased partial pressure or density of hydro-carbons close to the target surface due to e.g. a plasma plume (e.g. [32]). Experimental data for the ablation plume dynamics in a similar ablation regime show however that the cloud of ablated material expands in longitudinal direction with a velocity of $v = 10\,\mathrm{m/ms}$ [33]. A fast, directed expansion away from the target contradicts the assumption of a high-pressure region at the target surface on the time-scale of $\tau_{rec} \approx 90\,\mathrm{ms}$.
If the recovery of the contaminant layer is not due to the ablation plume, it must occur from the background pressure of e.g. water and hydro-carbons inside the experimental chamber. In that case, $\tau_{rec} \approx 90\,\mathrm{ms}$ measured in the presented experiment could indicate that in fact a much thinner contaminant layer is required to re-establish the non-ablated acceleration conditions. The thickness of the required source layer can be estimated from the impact rate R at the experimental conditions and the recovery time τ_{rec} measured in the experiment: For the experimental conditions, the proton source with the highest partial pressure is water with $p_{H_2O} = 2.3 \cdot 10^{-6}\,\mathrm{mbar}$ (residual gas analyzer measurement). Assuming room temperature and the mass of water, an impact rate of $R = 1.3 \cdot 10^{15}\,\mathrm{cm^{-2}\,s^{-1}}$ results. With a growth time $\tau_{rec} = 90\,\mathrm{ms}$ follows $N_{90ms} = 1.2 \cdot 10^{14}\,\mathrm{cm^{-2}}$ for the number of water molecules adsorbed at the surface per area, which corresponds to a surface coverage of 10% of a monolayer. This value is much less than the hydro-carbon layer actually present at the target surface according to measurements (see Tab. 2). The question is therefore whether a source layer of that thickness can provide a sufficient number of ions. Assuming a source size of $100\,\mu\mathrm{m}$ ($300/600\,\mu\mathrm{m}$) for particles accelerated from the target rear surface, for the number of particles within the source size holds: $2 \cdot 10^{10}$, $2 \cdot 10^{11}$ and $7 \cdot 10^{11}$, respectively. Comparison with the integral number of protons N_p contained in an accelerated pulse in the reference case (see Fig. 2a) of $N_p \approx 4 \cdot 10^{11}$ shows that a sufficient number of protons has re-adsorbed to the surface in $\tau_{rec} = 90\,\mathrm{ms}$ when a source diameter of $500\,\mu\mathrm{m}$ is assumed. The data summarized in Tab. 1 show that the estimated value of $500\,\mu\mathrm{m}$ is larger than most published values, but a proton source size $\sim 500\,\mu\mathrm{m}$ (lower limit) will be confirmed from a lateral source size estimation in the low-fluence ablation regime presented in Sec. 5.

5. Ablation-Based Source Size Characterization

For the low-fluence regime ($F \approx 0.6\,\mathrm{J/cm^2}$), the experiment was focused on the correlation between the spatial proton distribution in the source layer and the resulting angular distribution of accelerated protons. The data are firstly analyzed to confirm the source location - target front versus rear surface - for our TNSA conditions and secondly to estimate the proton source size at the target rear surface.

5.1. Source Location

To determine the source location, the proton signal from a 2 μm thick titanium foil was compared for the case without (reference case) and with surface cleaning. In the latter case, 95 consecutive ablation pulses were applied to the target front or rear surface at a repetition rate of 10 Hz with the last ablation pulse arriving at the target 5 ms prior to the arrival of the acceleration pulse. Fig. 4 summarizes the according proton beam profiles recorded on RCF stacks. The reference case shows proton energies above 13.4 MeV and a homogeneous beam profile with a weak asymmetry, which might be attributed to a residual pulse front tilt of the acceleration pulse [34]. For front surface ablation, a similarly homogeneous beam profile is recorded. Note that, compared to the reference case, the slightly lower maximum proton energy of 12.1 MeV is well in the range of shot-to-shot fluctuations observed during this and other experiments. The similarity between the reference and front side ablated proton data shows that the ablation process ending 5 ms prior to the acceleration pulse arrival does not influence the primary laser-target interaction conditions at the target front surface.
In contrast, the rear surface ablation shows a clear decrease in the maximum proton energy by about 50 % compared to the reference shot. In addition, a void becomes visible in the beam profile of the 4.7 MeV energy layer, i.e. a region where the proton yield or dose is strongly diminished. This data set confirms that the experiments are performed in the TNSA regime where the ion source for particles detected behind the target rear surface is located at the target rear surface [5, 10]. However, the relatively large ablation spot (400/600 μm diameter for $F > 0.9/0.5 \cdot F_{peak}$, see Fig. 1b) but remaining proton signal of high energies (> 7 MeV) in the case of rear surface ablation challenges the assumption of $\sim 100\,\mu$m large source sizes for TNSA (see Tab. 1).

5.2. Proton Emission Pattern and Source Size Estimation

In the well-established quasi-stationary picture of TNSA, the energy- and angle-resolved proton emission pattern as recorded on RCF is connected to the bell-shaped spatial distribution of the Debye sheath [11]. Protons are accelerated normal to iso-density surfaces within the Debye sheath [35], which determines the protons' final emission angle θ (laminar expansion [16]). This scenario is illustrated in Fig. 5a. According to the bell-shape of the sheath, the source position of a proton on the target surface and its emission angle are correlated [35]: emission along the target normal ($\theta = 0°$) occurs in the Debye sheath center and in the flat outer areas. Emission angles of $\theta > 0°$ are acquired by protons starting in the slope regions of the sheath. Moreover, the local maximum field strength determines the maximum proton energy that can be acquired from a source position. In summary, the shape and local field strength of the Debye sheath result in the typically observed decreasing proton source size and emission angle with increasing proton energy (compare Fig. 4a and Fig. 5a).
The experimentally observed proton emission pattern in the case of rear surface ablation (Fig. 4c) can be interpreted in the framework of this simple Debye sheath model (Fig. 5):

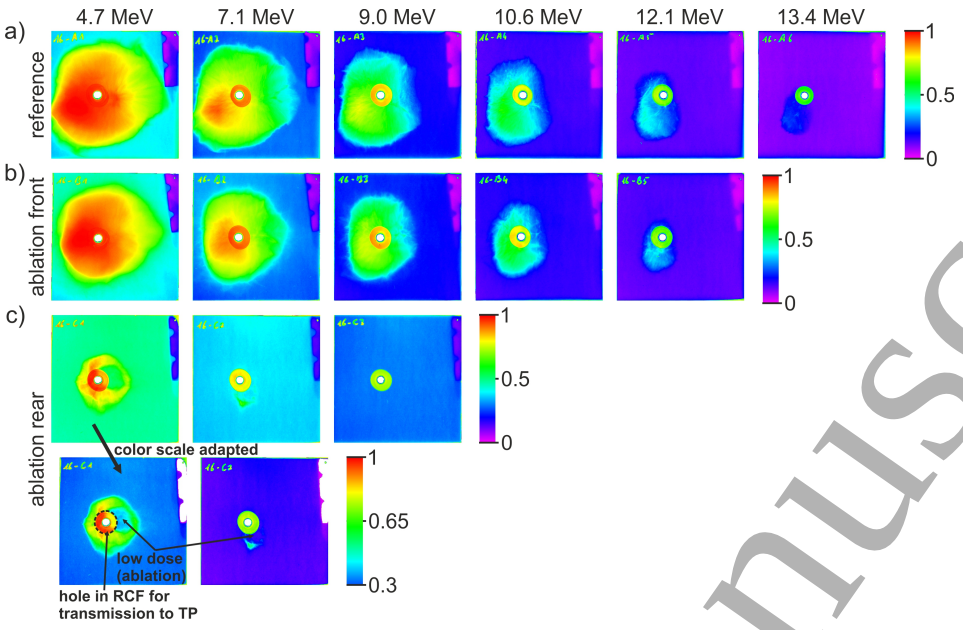

Figure 4. Low ablation fluence case. False-color representation of RCF without ablation (reference) and front and rear surface ablation. All RCF represented show single-shot proton pulse. The case of rear surface ablation is shown with two different color scales to firstly allow for the comparison with the reference case and secondly to increase the visibility of the ring-like proton emission. The measurements were done by applying 95 consecutive ablation shots with a fluence of $0.62\,\mathrm{J/cm^2}$ and $0.66\,\mathrm{J/cm^2}$ on the front and rear surface, respectively.

The lack of proton signal at energies $> 7.1\,\mathrm{MeV}$ compared to the reference case indicates that the source size for this proton energy range is smaller than the ablated spot size, i.e. all possible source ions are removed. On the other hand, the ring-like proton emission around the target normal direction (marked by the hole in the RCF layers) for the energy range around $4.7\,\mathrm{MeV}$ indicates that the source size for $4.7\,\mathrm{MeV}$ is larger than the ablated area.

A quantitative estimate for the source size at the target rear surface can be derived from the apparent connection between the spatially selective removal of the source layer with the decrease in proton yield in a specific solid angle. This method in principle borrows from the *direct imaging method* (see Tab. 1) for source size measurements: Geometric features on the target surface imprint into the angular distribution of protons during acceleration/laminar expansion and the source size is derived from the spatial extent of the illuminated and transported surface features [16]. In the experiments presented here, the geometric surface structures are replaced by an ablated area of known size. Since the exact threshold fluence for ablation in the multi-shot mode is unknown, the ablated spot size is estimated from the data presented in Fig. 1b. The plot shows that the ablation fluence F is constant over a radius $r = 200\,\mu\mathrm{m}$ and $\mathrm{F} \approx 0$ for $r > 450\,\mu\mathrm{m}$. To yield a lower limit as well as a range for the source size, it is assumed that removal of the contaminant/source layer by ablation occurs at least up to 90% of F_{peak}, i.e. over

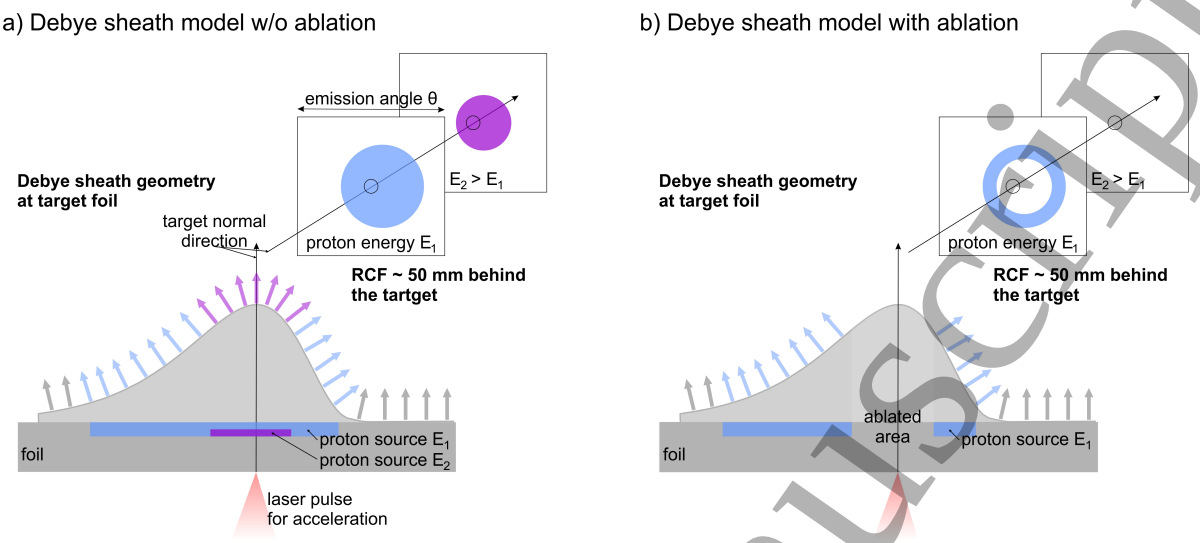

Figure 5. Debye sheath model without and with ablation. The model is simplified, merging the position-dependent field strength and the emission angle determined by the iso-density surfaces into a single sketch. a) The sketch illustrates the correlation of the Debye sheath shape (emission angles represented by colored arrows), particle source size and the resulting energy-dependent angular emission pattern of protons on an RCF stack ~50 mm behind the target. The Debye sheath is modeled with a skewness to account for the experimentally observed asymmetry in the proton emission pattern. b) Ablation of the source layer over a finite area results in a change in the proton emission patterns.

a radius of 200 μm (lower limit) or up to 50% of F_{peak}, corresponding to a radius of 300 μm.

Starting point for the ablation-based source size estimation method illustrated in Fig. 6 is the measured angular distribution of protons $dN/d\theta$ in a single RCF layer for the reference/non-ablated case (see Fig. 4) in combination with the well-characterized ablation spot. Since only a narrow proton energy range ΔE is considered (single RCF layer), $dN/d\theta$ is determined by the structure of the bell-shaped iso-density surface in the Debye sheath (Fig. 5), which maps a proton source position x along the surface to an emission angle θ.

The iso-density surface is here modeled as a skewed Gaussian mapping function $g_{x\to\theta}$ (Fig. 6b) and the proton emission angle $\theta(x)$ is given by the derivative of $g_{x\to\theta}$ at the position x (Fig. 6c). $\theta(x)$ is hence parameterized via the amplitude A, width σ and skewness b of $g_{x\to\theta}$, where the ratio A/σ and the parameter b are determined based on the envelope (maximum emission angle left/right from the $\theta = 0°$ direction) of the non-ablated $dN/d\theta$ distribution (see orange lines in Fig. 6a/c/e). The skewness b accounts for the off-target-normal proton emission centroid (see Fig. 4).

Based on the mapping function $g_{x\to\theta}$ for the non-ablated case, the angular proton distribution $dN/d\theta$ for the ablated case can consistently be generated when proton emission from the ablated region of 400/600 μm diameter is excluded: The smaller envelope of

the ablated angular proton distribution as well as the ring-like emission around $\theta = -10°$ are well reproduced (Fig. 6a/c/e). The precondition is that the Debye sheath as the origin of the angular proton distribution does not change during the ablation process. Under this assumption, the proton source size becomes accessible from the ablated data set as firstly, the ablation spot of known size introduces an absolute spatial scale in the proton source area and secondly, the ambiguity in the space-angle-correlation is removed (Fig. 6c/e) compared to the non-ablated case. In particular, the proton emission around $\theta = -10°$ can be mapped to a source location between $x = 200\,\mu$m and $x = 225\,\mu$m and $x = 300\,\mu$m and $x = 330\,\mu$m for ablation at $F > 0.9 \cdot F_{peak}$ and $F > 0.5 \cdot F_{peak}$, respectively (Fig. 6). For positive emission angles, however, the source size cannot be determined because the minimum emission angle is masked by the hole in the RCF stack along the target normal direction. The ablation-based method for the source size estimation hence yields a lower limit for the source diameter of $450\,\mu$m and indicates a range of up to $660\,\mu$m.

Discussion

Qualitatively, the ring-shaped proton emission after ablation indicates the validity of the simple model for the interplay of spatially-selective source layer removal by ablation and the TNSA process, as illustrated in Fig. 5. Since the model neglects any feedback of the ablation on the Debye sheath formation as well as dynamic effects, a possible interpretation of the agreement is that TNSA for ultra-short laser pulses is in fact strongly influenced by a pre-thermal acceleration phase [34], in which a static TNSA model is valid. This interpretation would be backed by the observed angular offset in the emission pattern, also ascribed to pre-thermal effects.

However, dynamic effects and an interplay between the ablation process and the accelerating field structure at the target rear surface cannot be excluded based on the given data set. For a change of the source size and hence the angular envelope of the proton distribution it is thereby not required that the actual source layer size changes but a local ablation-induced increase/decrease of the accelerating field in the Debye sheath can influence the proton energy range that a certain source location contributes to. In that case, the source size estimated from a data set with ablation could not be correlated with the non-ablated source size, hence leading to an over-/underestimation of the source size in the non-ablated case. Potential ablation-induced changes in the accelerating field structure and the correlated electron transport mechanisms will be a topic of future investigations.

A quantitative comparison of the presented source size estimation with published data is challenging as the published ion source size data for TNSA show a large variability (see Tab. 1). This variability should partly be the result of the different measurement techniques used. Moreover, the different TNSA-drive laser systems (pulse energy, pulse duration, focal spot quality) and targets applied in the experiments can be expected to

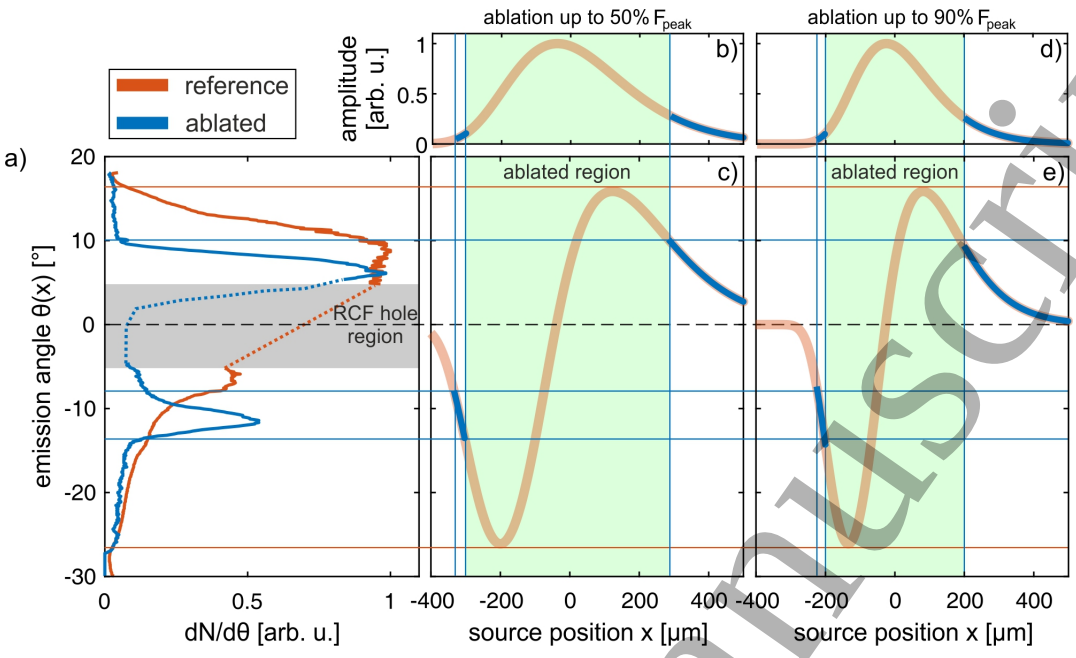

Figure 6. Ablation-based source size estimation for narrow proton energy class. a) Angle-resolved proton emission patterns $dN/d\theta$. The profiles are derived from RCF data for the reference/non-ablated case (orange) and the ablated case (blue) for a proton energy of 4.7 MeV (see Fig. 4a/c, profiles taken in horizontal direction). The region (RCF hole region) where the hole in the RCF stack masks the signal is marked and the profiles are interpolated in this region (dotted lines). b) The skewed Gaussian mapping function $g_{x\to\theta}$ projecting a source position x onto an emission angle $\theta(x)$ for a specific proton energy class, here 4.7 MeV. The 600 μm large ablated region ($F > 0.5 \cdot F_{peak}$) is marked. Whereas the lateral extent of the source size is undetermined in the reference case (orange trace), the source location and size for the ablated case (blue) can be derived from the angle-resolved proton emission patterns. c) Derivative of $g_{x\to\theta}$ and hence the emission angle $\theta(x)$. The orange/blue lines mark the emission regions which are in this way correlated with a source position. d/e) The subplots show the same scenario as b/c) but for an ablated spot size of 400 μm, i.e. ablation within a region where $F > 0.9 \cdot F_{peak}$.

influence the source sizes (e.g. electron refluxing). However, the published data do not show a clear trend in this regard and none of the drive-laser systems is comparable to the Draco laser system with which the presented results were collected.

Generally, it can be stated that the source size of 450 μm (lower limit) measured here is about 35% larger than formerly reported values (Tab. 1). That takes into account that the characterized energy layer of 4.7 MeV corresponds to only $\approx$30% of the maximum proton energy for the reference case (Fig.4a), i.e. a lower proton energy regime for which larger source sizes are reported in the published data. A comparison with established techniques (e.g. direct imaging of surface grooves [16]) applied to the ultra-short pulse laser regime ($\tau \leq 100$ fs, $E \sim 3$ J, $I \sim 10^{21}$ W/cm^2) could be useful to connect both – static and dynamic – approaches.

6. Conclusion

In summary, we have presented experimental results on ablation-based techniques for the proton source size characterization in the TNSA regime. The major result is that both applied experimental approaches (high- and low-fluence regime) independently indicate a lateral proton source size of $\approx 500\,\mu$m as a lower limit. This value exceeds formerly published data.

For the high-fluence case, the recovery time for the proton signal after rear-surface ablation allows to estimate that a hydro-carbon surface coverage of only 1/10 monolayer is sufficient to yield acceleration performance as in the non-ablated case. With this sparse surface coverage, a source area of at least $500\,\mu$m diameter contains the integral number of protons in the accelerated pulse. The observation that TNSA is operating for much thinner source layers than generally present on the target surfaces also shows the robustness of the acceleration mechanism.

In a second part of the study, the lateral source layer extent was estimated based on the correlation of a spatially-selective source layer removal at the target rear surface and the angular emission pattern of the proton distribution. Analysis of the experimental data based on a simple analytic model for the correlation of the source geometry and the proton emission pattern yielded a source diameter between $450\,\mu$m (lower limit) and $660\,\mu$m (range estimation) for protons at $\approx 30\%$ of the maximum proton energy achieved without ablation. This ablation-based approach for the source size measurement employs direct surface imaging but it is in contrast to surface imaging methods with e.g. grooved targets [16] applicable to any target type without further engineering. The method only requires an energy- and angle-resolved measurement of an ion distribution (e.g. from RCF), in which the ablation of an area of known size is reflected in the angular distribution.

Regarding an understanding of TNSA, the effect of the source layer thickness and its lateral extent e.g. on the acceleration performance of mass-limited targets [12] or the influence on multi-species effects require attention from simulations as well as experiments. However, the large lateral source sizes derived in the presented experiments might be challenging to realize even in state-of-the-art particle-in-cell simulations.

7. Acknowledgements

We would like to thank the Draco laser team with Stefan Bock, Uwe Helbig and René Gebhardt. Moreover, we would like to acknowledge the support from Dr. Roman Böttger from HZDR who provided scanning electron microscopy images of our ablated targets.

[1] H. Daido, M. Nishiuchi, and A. S. Pirozhkov. Review of laser-driven ion sources and their applications. *Reports on Progress in Physics*, 75(5):056401, 2012.

[2] S. P. Hatchett, C. G. Brown, T. E. Cowan, E. A. Henry, J. S. Johnson, M. H. Key, J. A. Koch, A. Bruce Langdon, B. F. Lasinski, R. W. Lee, A. J. Mackinnon, D. M. Pennington, M. D. Perry, T. W. Phillips, M. Roth, T. C. Sangster, M. S. Singh, R. A. Snavely, M. a. Stoyer, S. C. Wilks,

and K. Yasuike. Electron, photon, and ion beams from the relativistic interaction of Petawatt laser pulses with solid targets. *Physics of Plasmas*, 7(1999):2076, 2000.

[3] R. A. Snavely, M. H. Key, S. P. Hatchett, T. E. Cowan, M. Roth, T. W. Phillips, M. A. Stoyer, E. A. Henry, T. C. Sangster, M. S. Singh, S. C. Wilks, A. MacKinnon, A. Offenberger, D. M. Pennington, K. Yasuike, A. B. Langdon, B. F. Lasinski, J. Johnson, M. D. Perry, and E. M. Campbell. Intense High-Energy Proton Beams from Petawatt-Laser Irradiation of Solids. *Physical Review Letters*, 85(14):2945–2948, 2000.

[4] S. C. Wilks, A. B. Langdon, T. E. Cowan, M. Roth, M. Singh, S. Hatchett, M. H. Key, D. Pennington, A. MacKinnon, and R. a. Snavely. Energetic proton generation in ultra-intense laser-solid interactions. *Physics of Plasmas*, 8(2001):542–549, 2001.

[5] M. Allen, P. K. Patel, A. Mackinnon, D. Price, S. Wilks, and E. Morse. Direct Experimental Evidence of Back-Surface Ion Acceleration from Laser-Irradiated Gold Foils. 265004:1–4, 2004.

[6] S. Steinke, A. Henig, M. Schnürer, T. Sokollik, P. V. Nickles, D. Jung, D. Kiefer, R. Hörlein, J. Schreiber, T. Tajima, X. Q. Yan, M. Hegelich, J. Meyer-ter Vehn, W. Sandner, and D. Habs. Efficient ion acceleration by collective laser-driven electron dynamics with ultra-thin foil targets. *Laser and Particle Beams*, 28(01):215–221, 2010.

[7] M. Hegelich, S. Karsch, G. Pretzler, D. Habs, K. Witte, W. Guenther, M. Allen, A. Blazevic, J. Fuchs, J. C. Gauthier, M. Geissel, P. Audebert, T. E. Cowan, and M. Roth. MeV Ion Jets from Short-Pulse-Laser Interaction with Thin Foils. *Physical Review Letters*, 89(8):85002, 2002.

[8] B. M. Hegelich, B. J. Albright, J. Cobble, K. Flippo, S. Letzring, M. Paffett, H. Ruhl, J. Schreiber, R. K. Schulze, and J. C. Fernandez. Laser acceleration of quasi-monoenergetic MeV ion beams. *Nature*, 439(7075):441–444, 2006.

[9] S. Karsch, S. Düsterer, H. Schwoerer, F. Ewald, D. Habs, M. Hegelich, G. Pretzler, A. Pukhov, K. Witte, and R. Sauerbrey. High-Intensity Laser Induced Ion Acceleration from Heavy-Water Droplets. *Physical Review Letters*, 91(1):015001, 2003.

[10] J. Fuchs, Y. Sentoku, S. Karsch, J. Cobble, P. Audebert, A. Kemp, A. Nikroo, P. Antici, E. Brambrink, A. Blazevic, E. M. Campbell, J. C. Fernández, J.-C. Gauthier, M. Geissel, M. Hegelich, H. Pépin, H. Popescu, N. Renard-LeGalloudec, M. Roth, J. Schreiber, R. Stephens, and T. E. Cowan. Comparison of laser ion acceleration from the front and rear surfaces of thin foils. *Physical review letters*, 94(4):045004, 2005.

[11] J. Fuchs, T. E. Cowan, P. Audebert, H. Ruhl, L. Gremillet, A. Kemp, M. Allen, A. Blazevic, J. C. Gauthier, M. Geissel, M. Hegelich, S. Karsch, P. Parks, M. Roth, Y. Sentoku, R. Stephens, and E. M. Campbell. Spatial Uniformity of Laser-Accelerated Ultrahigh-Current MeV Electron Propagation in Metals and Insulators. *Physical Review Letters*, 91(25):255002, 2003.

[12] K. Zeil, J. Metzkes, T. Kluge, M. Bussmann, T. E. Cowan, S. D. Kraft, R. Sauerbrey, B. Schmidt, M. Zier, and U. Schramm. Robust energy enhancement of ultrashort pulse laser accelerated protons from reduced mass targets. *Plasma Physics and Controlled Fusion*, 56(8):084004, 2014.

[13] H. Schwoerer, S. Pfotenhauer, O. Jackel, K. U. Amthor, B. Liesfeld, W. Ziegler, R. Sauerbrey, K. W. D. Ledingham, and T. Esirkepov. Laser-plasma acceleration of quasi-monoenergetic protons from microstructured targets. *Nature*, 439(7075):445–448, 2006.

[14] S. M. Pfotenhauer, O. Jäckel, A. Sachtleben, J. Polz, K. W. D. Ledingham, R. Sauerbrey, P. Gibbon, A. P. L. Robinson, H. Schwoerer Spectral shaping of laser generated proton beams. *New Journal of Physics*, 10:1–14, 2008.

[15] J. C. Fernández, B. M. Hegelich, J. A. Cobble, K. A. Flippo, S. A. Letzring, R. P. Johnson, D. C. Gautier, T. Shimada, G. A. Kyrala, Y. Wang, C. J. Wetteland, and J. Schreiber. Laser-ablation treatment of short-pulse laser targets: Toward an experimental program on energetic-ion interactions with dense plasmas. *Laser and Particle Beams*, 23(03):267–273, 2005.

[16] T. E. Cowan, J. Fuchs, H. Ruhl, A. Kemp, P. Audebert, M. Roth, R. Stephens, I. Barton, A. Blazevic, J. C. Gauthier, M. Geissel, M. Hegelich, J. Kaae, S. Karsch, E. Brambrink, J. Cobble, J. Ferna, J. Fernandez, J. C. Gauthier, M. Geissel, M. Hegelich, J. Kaae, S. Karsch, G. P. Le Sage, S. Letzring, M. Manclossi, S. Meyroneinc, A. Newkirk, H. Pepin, N. Renard Legalloudec,

and J. Ferna. Ultralow Emittance, Multi-MeV Proton Beams from a Laser Virtual-Cathode Plasma Accelerator. *Physical Review Letters*, 92(20):204801, 2004.

[17] M. Roth, M. Allen, P. Audebert, A. Blazevic, E. Brambrink, T. E. Cowan, J. Fuchs, J.-C. Gauthier, M. Geissel, M. Hegelich, S. Karsch, J. Meyer-ter Vehn, H. Ruhl, T. Schlegel, and R. B. Stephens. The generation of high-quality, intense ion beams by ultra-intense lasers. *Plasma Physics and Controlled Fusion*, 44(12B):B99–B108, 2002.

[18] P. K. Patel, A. J. Mackinnon, M. H. Key, T. E. Cowan, M. E. Foord, M. Allen, D. F. Price, H. Ruhl, P. T. Springer, and R. Stephens. Isochoric heating of solid-density matter with an ultrafast proton beam. *Physical review letters*, 91:125004, 2003.

[19] H. Ruhl, T. Cowan, and J. Fuchs. The generation of micro-fiducials in laser-accelerated proton flows, their imaging property of surface structures and application for the characterization of the flow. *Physics of Plasmas*, 11(5 PART 1), 2004.

[20] F. Nürnberg, M. Schollmeier, E. Brambrink, A. Blažević, D. C. Carroll, K. Flippo, D. C. Gautier, M. Geissel, K. Harres, B. M. Hegelich, O. Lundh, K. Markey, P. McKenna, D. Neely, J. Schreiber, and M. Roth. Radiochromic film imaging spectroscopy of laser-accelerated proton beams. *Review of Scientific Instruments*, 80(2009), 2009.

[21] M. Borghesi, A. J. Mackinnon, D. H. Campbell, D. G. Hicks, S. Kar, P. K. Patel, D. Price, L. Romagnani, A. Schiavi, and O. Willi. Multi-MeV Proton Source Investigations in Ultraintense Laser-Foil Interactions. *Physical Review Letters*, 92:1–4, 2004.

[22] J. Schreiber, M. Kaluza, F. Grüner, U. Schramm, B. M. Hegelich, J. Cobble, M. Geissler, E. Brambrink, J. Fuchs, P. Audebert, D. Habs, and K. Witte. Source-size measurements and charge distributions of ions accelerated from thin foils irradiated by high-intensity laser pulses. *Applied Physics B: Lasers and Optics*, 79(8 SPEC. ISS.):1041–1045, 2004.

[23] J. Schreiber, S. Ter-Avetisyan, E. Risse, M. P. Kalachnikov, P. V. Nickles, W. Sandner, U. Schramm, D. Habs, J. Witte, and M. Schnürer. Pointing of laser-accelerated proton beams. *Physics of Plasmas*, 13:033111, 2006.

[24] E. Brambrink, J. Schreiber, T. Schlegel, P. Audebert, J. Cobble, J. Fuchs, M. Hegelich, and M. Roth. Transverse characteristics of short-pulse laser-produced ion beams: A study of the acceleration dynamics. *Physical Review Letters*, 96(15):1–4, 2006.

[25] M. Roth, P. Audebert, A. Blazevic, E. Brambrink, J. Cobble, T. E. Cowan, J. Fernandez, J. Fuchs, M. Geissel, M. Hegelich, S. Karsch, H. Ruhl, M. Schollmeier, and R. Stephens. Laser accelerated heavy particles - Tailoring of ion beams on a nano-scale. *Optics Communications*, 264(2):519–524, 2006.

[26] P. McKenna, D. C. Carroll, R. J. Clarke, R. G. Evans, K. W D Ledingham, F. Lindau, O. Lundh, T. McCanny, D. Neely, A. P L Robinson, L. Robson, P. T. Simpson, C. G. Wahlström, and M. Zepf. Lateral electron transport in high-intensity laser-irradiated foils diagnosed by ion emission. *Physical Review Letters*, 98(14):1–4, 2007.

[27] S. Ter-Avetisyan, M. Schnürer, P. V. Nickles, W. Sandner, T. Nakamura, and K. Mima. Correlation of spectral, spatial, and angular characteristics of an ultrashort laser driven proton source. *Physics of Plasmas*, 16(4):10–16, 2009.

[28] B. N. Chichkov, C. Momma, S. Nolte, F. von Alvensleben, A. Tünnermann. Femtosecond, picosecond and nanosecond laser ablation of solids. *Applied Physics A Materials Science & Processing*, 63:109–115, 1996.

[29] L. Torrisi, A. Borrielli, and D. Margarone. Study on the ablation threshold induced by pulsed lasers at different wavelengths. *Nuclear Instruments and Methods in Physics Research, Section B: Beam Interactions with Materials and Atoms*, 255(2):373–379, 2007.

[30] Y. Jee, F. M. Becker, and M. R. Walser. Laser-induced damage on single-crystal metal surfaces. *J. Opt. Soc. Am. B*, 5(3):648–659, 1988.

[31] F. Dollar, T. Matsuoka, G. M. Petrov, A. G. R. Thomas, S. S. Bulanov, V. Chvykov, J. Davis, G. Kalinchenko, C. Mcguffey, L. Willingale, V. Yanovsky, A. Maksimchuk, and K. Krushelnick. Control of Energy Spread and Dark Current in Proton and Ion Beams Generated in High-

Contrast Laser Solid Interactions. *Physical Review Letters*, 065003:1–5, 2011.

[32] K. B. Wharton, C. D. Boley, A. M. Komashko, A. M. Rubenchik, J. Zweiback, J. Crane, G. Hays, T. E. Cowan, and T. Ditmire. Effects of nonionizing prepulses in high-intensity laser-solid interactions. *Physical Review E*, 64:025401(R), 2001.

[33] D. B. Geohegan. Fast intensified-CCD photography of YBa2Cu3O 7-x laser ablation in vacuum and ambient oxygen. *Applied Physics Letters*, 60(22):2732–2734, 1992.

[34] K. Zeil, J. Metzkes, T. Kluge, M. Bussmann, T. E. Cowan, S. D. Kraft, R. Sauerbrey, and U. Schramm. Direct observation of prompt pre-thermal laser ion sheath acceleration. *Nature Communications*, 3:874, 2012.

[35] M. Borghesi, J. Fuchs, S. V. Bulanov, A. J. MacKinnon, P. K. Patel, and M. Roth. Fast Ion Generation by High-Intensity Laser Irradiation of Solid Targets and Applications. *Fusion Science and Technolog*, 49:412–439, 2006.